Imprint on the upper mantle discontinuities of a subducted Paleo-Tethys oceanic lithosphere and the formation of the Emeishan large igneous province

Chuansong He[1*]

[1]*Institute of Geophysics, China Earthquake Administration, Beijing 100081, China*

Abstract:

Generally, it is suggested that mantle plume upwelling led to the formation of the Emeishan large igneous province (ELIP). However, this notion has been challenged by recent geological and seismic studies. In this study, 3 profiles of velocity perturbation crossing the ELIP were drawn following previous tomography, and common conversion point (CCP) stacking of receiver functions is carried out in the ELIP. The slab-like high-velocity structure with northeastward subduction is revealed, which may be associated with an oceanic lithosphere of the Paleo-Tethys (OLPT). CCP stacking of receiver functions shows that the OLPT generated an imprint on the 410 and 660 km discontinuities, respectively. Finally, it is suggested that the OLPT may induce large-scale return flow or upwelling of the mantle, which contributed to the formation of the ELIP.

* Corresponding author: hechuansong@aliyun.com

Key words: CCP stacking of receiver function; upper mantle discontinuity; tomography; Oceanic lithosphere of the Paleo-Tethys; mantle upwelling; Emeishan large igneous province

1. Introduction

Mantle dynamics are closely influenced by vast and transient magmatic eruptions or outpourings, which have occurred throughout geological history around the globe (Ernst and Buchan, 2001; Coffin and Eldholm, 2001). Mantle plumes rooted in the lower mantle are generally considered (Wilson, 1963) to have generated several large igneous (magmatic) provinces, such as the ELIP of China, the Siberian traps and the Deccan large igneous province of India (Uenzelmann-Neben, 2013; Pirajno and Hoatson, 2012; Ernst et al., 2019; Zhu et al., 2020). This process has been invoked to explain great environmental changes on the Earth's surface and mass extinctions in the Permian (Buiter, 2014; Wignall, 2011).

The ELIP, which formed from 263 to 260 Ma (Liu & Zhu 2009), is exposed over 250,000-300,000 km^2 in Southwest China, includes 250,000 km^3 of basaltic flows (Deng et al., 2010; Ali et al., 2010; Wu et al., 2018; Xu et al., 2018) (Fig. 1) and is one of most well-known large igneous provinces in the world. Reports have proposed that the ELIP may be linked with a later Permian mantle plume, and based on geochemical, biostratigraphic, and sedimentological characteristics, the ELIP is divided into inner,

middle and outer zones (Fig. 1, left panel) (Xu et al., 2001; Deng et al., 2010).

However, recent geological studies discovered that certain lava flows erupted in a submarine setting near the inner zone of the ELIP (Ukstins Peate and Bryan, 2008), and several lava outcrops also formed at low elevations at the boundary of the inner and middle uplift zones (Ukstins Peate and Bryan, 2008). These results challenge the mantle plume model because numerical simulations have demonstrated that mantle plume upwelling should have induced a 0.5–2 km broad dome uplift with an ~1000 km diameter (Ernst et al., 2005; Sengör, 2001; Griffiths and Campbell, 1991).

Generally, mantle upwelling and lower crustal/lithospheric delamination (or a subducting slab) in early Earth history can retain high- and low-velocity vestiges, which can be preserved for two billion years or longer (Balling et al., 2000; Cook et al., 1999; Zhai et al., 2007; Zhao et al., 1992; He et al., 2015; Xu et al., 2004; Anderson, 1982) and be detected by seismic techniques (Wu et al., 1994; Deng et al., 2004; He and Santosh, 2021).

However, recent receiver functions and tomographic studies have not revealed any relics of mantle plume upwelling in the ELIP (He et al., 2014; He and Santosh, 2020). On contrary, tomography revealed large-scale low-velocity anomaly (or mantle upwelling) in the upper mantle rather than rooted from core-mantle boundary (He and Santosh, 2020). Meanwhile, receiver function (He, 2010) and tomographic studies (Huang et al., 2015;

Yang et al., 2014; He and Santosh, 2017；2020) have revealed a vestige with subducted slab-like features in this area. However, previous receiver function studies only used a set of extremely limited data and obtained images of CCP stacking of receiver functions with low signal and noise ratios (He, 2010), and the detailed structure of the mantle transition zone (MTZ) is very obscure. Another receiver function study only used the depth domain receiver function to image the 410 and 660 km discontinuities with 446 teleseismic events (He et al., 2014), which did not remove the effect of velocity heterogeneities in the upper mantle; the depth of discontinuities only is pseudo depth. Although recent CCP stacking of receiver function used much data collected from the mobile seismic stations, the valid receiver function may be quite limited so that some important detail feature cannot be revealed, such as split 410 and 660 km discontinuities (e.g., Xu et al., 2018; Zhang et al., 2017), moreover, their works didn't involve the sudducted slab and the formation of the ELIP.

In this study, the tomographic images (He and Santosh, 2020) are redrawn and reanalyzed and CCP stacking of receiver functions is performed by using a 3-D velocity mode that is used to remove the effect of velocity heterogeneities of the upper mantle. Three velocity perturbations and CCP stacking of receiver function profiles crossing the ELIP are created. The results affirm that there is a subducted lithosphere of the Paleo-Tethys beneath the ELIP, which might play a key role in ELIP formation.

2. Data and method

A total of 1407 teleseismic events were collected from 177 permanent seismic stations during 2007 to 2020 in Southwest China (Fig. 1). The events were limited to Ms >6.0, and the earthquake epicentral distances ranged from 30° to 90° for individual event-station pairs. The raw waveforms with a 50 Hz or 100 Hz sampling rate were cut from 15 s before the P-wave arrival time to 150 s after it and filtered by a Butterworth bandpass filter ranging from 0.01 to 0.2 Hz; the sample rate of the waveform was decimalized to 0.1 s increments. The waveform cross-correlation technique (VanDecar and Crosson, 1990) was employed to select consistent raw data (an example can be found in Fig. S1). The 1 s Gaussian factors and 0.01 water levels were adopted to compute the receiver functions (Langston, 1977; Owens et al., 1984). Finally, 20910 high-quality and valid receiver functions were extracted and used to CCP stacking of receiver function (for example, please see Fig. S2), which is far beyond any dataset of the previous receiver function studies in this area (e.g., Xu et al., 2018; Zhang et al., 2017).

A CCP stacking of receiver functions (e.g., Dueker and Sheehan, 1997; Eagar et al., 2010; Zhu, 2000) was used to stack receiver functions and image the MTZ of the ELIP. The piercing points of receiver functions at 410 and 660 km depths are calculated by using the AK135 1-D velocity model (Kennett et al., 1995). The spherical coordinates are used to calculate the Ps–P differential time T_{Ps} (Eagar et al., 2010). The effect of velocity heterogeneities of the upper mantle is removed by a global 3-D velocity model (TX2019slab S- and P-wave velocity model) (Lu et al., 2019). Lateral grid intervals of 0.5°

and depth intervals of 1 km are designed for the CCP stacking process of receiver functions and the migrated receiver functions are searched within a radius of 75 km (Xu et al., 2018).

3. Results

The tomography results has been redrawn (He and Santosh, 2020) and reveals a subducted slab-like body of high velocity (SSBHV) beneath the southwestern ELIP (Fig. 2, B). The results identified by the CCP stacking of receiver functions show four interfaces corresponding to the location of the subducted slab, which are at depths of approximately 390, 400, 420 and 430 km (Fig. 2C,② , ③ , ④ and ⑤; Fig. 2). The 660 km discontinuity splits two or three interfaces, which deepens and is dislocated by approximately 30 km compared with the normal depth of the 660 km discontinuity at the location of the subducted slab (Fig. 2C, Fig. 2B).

Previous seismic studies indicate that the decreasing temperature can induce the split 520 km discontinuity (or two 520 km discontinuities) (Saikia et al., 2008; Deuss and Woodhouse, 2001). The high-velocity anomaly (or subducted slab) (Fig. 2B) might be linked to a lower temperature than that of the surrounding mantle (Foulger, 2012). Therefore, foure interfaces at 390-430 km depth might be connected to the split 410 km discontinuity. Recent CCP stacking of receiver function in the South China also defined split 410 km discontinuity induced by a high-velocity anomaly (He and Santosh, 2021). Similarly, the deepening region of the 660 km discontinuity and split 660 km discontinuity

identified in this study might be also generated by the subducted slab due to its lower temperature than the high-velocity surrounding mantle (Foulger, 2012).

The X-discontinuity in the range of 250–350 km depth have reported from several seismological investigations (Deuss and Woodhouse, 2002, 2004; Revenaugh and Jordan, 1991). A large amplitude discontinuity identified in this study appears at 250 km depth (Fig. 2C, ①), which most likely represent an X-discontinuity, moreover, the discontinuity well correspond to the location of the low-velocity anomaly (Lv1).

Overlapping figures of the P-wave perturbation and CCP stacking of receiver function profiles further indicate the split 660 km discontinuity corresponding to a SSBHV (Fig. 3, the region within the blue ellipse), whereas the that of the X-discontinuity corresponding to the low velocity anomaly (Fig. 3, the region within the blue rectangle).

The topographies of the 410 and 660 km discontinuities have been extracted. The shallowing of the 410 km discontinuity (Fig. 4e, blue rectangle region) and the deepening of the 660 km discontinuity (Fig. 4f, blue rectangle region) correspond to the location of the SSBHV. On the other hand, the topographies of the 410 and 660 km discontinuities have also been extracted by using a local 3-D P-wave velocity model (He and Santosh, 2020) and inferred the S-wave velocity based on the Vp/Vs ratio of the AK135 velocity model correction (Kennett et al., 1995) (Fig. 5). Results show that the shallowing of the 410 km discontinuity (Fig. 5a, blue rectangle region) and the deepening of the 660 km

discontinuity (Fig. 5b, blue rectangle region) correspond to the location of the SSBHV. Finally, the thickness of the MTZ is extracted by used two kind velocity model corrections (Lu et al., 2019; He and Santosh, 2020) (Fig. 6). Results indicate that the thinning region of the MTZ (blue rectangle region) corresponding to the SSBHV (Fig. 2, Fig. 3 and Fig. 6).

Seismic studies has reported the 410 km discontinuity has positive Clapeyron slope, whereas that of the 660 km discontinuity has negative Clapeyron slope due to the phase change (e.g., van der Meijde et al., 2005; Bina and Helffrich, 1994). When the temperature decreased, the depth of the 410 km discontinuity respond to a shallowing topography, whereas that of the 660 km discontinuity reflect a deepening topography. Therefore, the thinning region of the MZT might be imprint of the subducted slab.

4. Subducted oceanic lithosphere of the Paleo-Tethys

The Ailaoshan suture is a Paleo-Tethys suture (Metcalfe, 2013), and the amalgamation time of the suture is ca. 245 Ma (Reid et al., 2007; Xu et al., 2015), which nearly overlaps with the formation time of the ELIP. Geological studies have indicated that the ELIP was cut by several strike-slip faults due to the latest phase of orogeny, particularly the Red River Fault (or Ailaoshan suture) (Wang et al. 1998; Leloup et al. 1995) (Fig. 1, the Red River Fault located in the inner zone of the ELIP). These changes led to the transport of a number of fragments in the western part of the ELIP several hundred kilometers to the southeast, including the terranes that are now exposed in northwestern Vietnam and

176 nearby regions (Wang et al. 1998; Leloup et al. 1995). Accordingly, the formation of the
177 ELIP likely occurred later than the closure of the Paleo-Tethys Ocean and may have been
178 linked to the closure of the Paleo-Tethys Ocean.
179
180 The Sanjiang Tethys zone of China (Fig. 1) belongs to the eastern Tethyan tectonic
181 belt, including the Ailaoshan suture (or Red River Fault), which retains the tectonic
182 evolutionary vestige of the Tethyan tectonic belt in Southeast Asia within the convergent
183 plate margin (Deng et al., 2014; Zi et al., 2012; Fan et al., 2010). This belt evolved through
184 the subduction of the oceanic plate and the process of continent–continent collision (Mo et
185 al., 2001; Metcalfe, 2013; Wang et al., 2014; Pan et al., 2012). In particular, the
186 Paleo-Tethyan Ocean plate subducted beneath the Eurasian plate, accompanied by
187 Paleo-Tethyan Ocean closure during the Paleozoic–Mesozoic (Hou et al., 2007; Hennig et
188 al., 2009; Chatterjee et al., 2012; Mo et al., 1998; Song et al., 2017; Shen et al., 2018; Xu
189 et al., 2019).
190
191 Thus, the subducted SSBHV identified by tomography (Figs. 2B) might belong to a
192 subducted OLPT. Although some workers suggest the possibility that the subducted
193 Indian plate contributes SSBHV (Huang et al., 2015; Xu et al., 2018; Lei et al., 2019),
194 geological, geochronological and tectonic investigations indicate that the
195 northeastward-subducted slab in this area is mainly related to the Paleo-Tethys tectonic
196 domain rather than the Indian plate (Weislogel, 2008; Liu and Xia, 2015; L Zhang et al.,
197 2007; iu and Xia, 2015; Peng et al., 2013; Liu et al., 2000). Moreover, the Indian plate

mainly subducted or moved northward, which is different from the subducted direction of the SSBHV defined by the present study. Specially, the extensive distribution of the later Paleozoic-Mesozoic igneous rocks in the Sanjiang Tethys region (Zhang et al., 2007; Weislogel, 2008; Liu and Xia, 2015; Liu and Xia, 2015; Peng et al., 2013) that might be linked to the subducted slab, which further demonstrates the subducted slab might belong to the OLPT.

5. Return flow and upwelling of the mantle

In assembled plate marginal regions, oceanic plates (lithospheric) subducted into the MTZ, resulting in a return flow or upwelling of mantle (Zhao and Ohtani, 2009; Santosh et al., 2010; Garfunkel, 1975), forming convective circulation in the upper mantle that leads to strong and extensive crust-mantle interactions (or melting of such metasomatized mantle) and magmatic activities (Kou et al., 2012; Wilson, 1989). Kincaid et al. (2013) reported the results of a mantle upwelling simulation in a subduction zone and indicated that the subducting slab can generate large-scale mantle flow. Multiline studies also suggested that some typical flood basalt provinces might be generated by subduction processes (Strak and Schellart, 2018), such as the Siberian Traps large igneous province (e.g., Ivanov and Litasov, 2013; Ivanov et al., 2008) and Columbia River flood basalts (e.g., Cabato et al., 2015; Stefano et al., 2011).

Large-scale low-velocity anomalies (Lv1) in the ELIP is just above the OLPT, which

most likely belong to the vestiges of the return flow of the mantle (or mantle upwelling) induced by the subducted OLPT (Fig. 2B). If it that is right, the subducted OLPT or return flow of the mantle might have played a key role in the formation of the ELIP (Fig. 7).

Recent geochemical and petrological studies also indicated that interaction between the mantle upwelling and the subduction system of the Paleo-Tethyan in the ELIP (Xu et al., 2019; Wang et al., 2018; Yang et al., 2019; Xu et al., 2019), which do not exclude the northeastward subduction of the OLPT along the Sanjiang Tethys zone (Liu et al., 2000) led to the mantle upwelling.

6. Conclusions

Tomography and CCP stacking of receiver functions demonstrated that there is a remnant of the Paleo-Tethyan lithosphere that subducted northeastward or beneath the ELIP along the Sanjiang Tethys zone accompanied by Paleo-Tethyan Ocean closure. The subduction of the Paleo-Tethyan Plate can generate return flow or upwelling of the mantle, which may have played a key role in ELIP formation. Meanwhile, interesting findings show that a subducted slab can lead to a split 410 km discontinuity and 660 km discontinuities, whereas the low velocity anomaly can enhance the X-discontinuity, which is the first such discovery in the geoscience field.

Acknowledgments

Thanks to the National Key R&D Plan of China (2017YFC601406) and the Data Management Center of the China National Seismic Network at the Institute of Geophysics and the China Earthquake Networks Centre. The CCP stacking data of receiver functions can be accessed via https://doi.org/10.5281/zenodo.3716248.

References

Ali, J.R., Fitton, J.G., Herzberg, C., 2010. Emeishan large igneous province (SW China) and the mantle-plume up-doming hypothesis. Journal of the Geological Society 167, 953-959.

Anderson, D.L., 1982. Hotspots, polar wander, mesozoic convection, and the geoid. Nature 297, 391-393.

Balling, N., 2000. Deep seismic reflection evidence for ancient subduction and collision zones within the continental lithosphere of northwestern Europe: Tectonophysics 329, 269-300.

Bina, C., Helffrich, G., 1994. Phase transition Clapeyron slopes and transition zone seismic discontinuity topography: Journal of Geophysics Research 99 (B8), 15853-15860.

Buiter, S., 2014. How plumes help to break plates. Nature 513, 36-37.

Cabato, J.A., Stefano, C.J., Mukasa, S.B., 2015. Volatile concentrations in olivine-hosted

melt inclusions from the Columbia River flood basalts and associated lavas of the Oregon Plateau: Implications for magma genesis. Chem. Geol. 392, 59-73.

Chatterjee, S., Goswami, A., Scotese, R., 2013. The longest voyage: tectonic, magmatic and paleoclimatic evolution of the Indian plate during its northward flight from Gondwana to Asia. Gondwana Research 23, 238-267.

Cook, F.A., Velden, A., Hall, K.W., Roberts, B., 1999. Frozen subduction in Canadas Northwest Territories: lithoprobe deep lithospheric reflection profiling of the western Canadian Shield. Tectonics 18, 1-24.

Coffin, M.F., Eldholm, O., 2001. Large igneous provinces: progenitors of some ophiolites. In: Ernst, R.E., Buchan, K.L. (Eds.), Mantle Plumes: Their Identification through Time. : Special Paper, 352. Geological Society of America, pp. 59-70.

Data Management Centre of China National Seismic Network. Waveform data of China National Seismic Network. Institute of Geophysics, China Earthquake Administration, 2007, doi:10.11998/SeisDmc/SN, http://www.seisdmc.ac.cn.

Deng, J.F., Mo, X.X., Zhao, H.L., Wu, Z.X., Luo, Z.H., Su, S.G., 2004. A new model for the dynamic evolution of Chinese lithosphere: ‘continental roots–plume tectonics’. Earth-Science Reviews 65, 223-275.

Deng, J., Wang, Q.F., Li, G.J., Li, C.S., Wang, C.M., 2014. Tethys evolution and spatial temporal distribution of ore deposits in the Sanjiang region, Southwestern China. Gondwana Res. 26, 419-437.

Deng, J., Wang, Q.F., Yang, S.J., Liu, X.F., Zhang, Q.Z., Yang, L.Q., Yang, Y.H., 2010. Genetic relationship between the Emeishan plume and the bauxite deposits in

286 Western Guangxi, China: Constraints from U–Pb and Lu–Hf isotopes of the detrital
287 zircons in bauxite ores. Journal of Asian Earth Sciences 37, 412-424.
288 Deuss, A., Woodhouse, J., 2001. Seismic Observations of Splitting of the Mid-Transition
289 Zone Discontinuity in Earth‘s Mantle. Science 294, 354-357.
290 Deuss, A., Woodhouse, J.H., 2002. A systematic search for upper mantle discontinuities
291 using SS-precursors, Geophys. Res. Lett. 29, 90(1)-90(4).
292 Deuss, A., Woodhouse, J.H., 2004. The nature of the Lehmann discontinuity from its
293 seismological Clapeyron slopes. Earth and Planetary Science Letters 225, 295-304.
294 Dueker, K.G., Sheehan, A.F., 1997. Mantle discontinuity structure from midpoint stacks of
295 converted P to S waves across the Yellowstone hotspot track. J. Geo-phys. Res.,
296 Solid Earth102, 8313-8327.
297 Eagar, K.C., Fouch, M.J., James, D.E., 2010. Receiver function imaging of upper man-tle
298 complexity beneath the Pacific Northwest, United States. Earth Planet. Sci. Lett.297,
299 141-153.
300 Ernst, R.E., Buchan, K.L., 2001. Large mafic magmatic events through time and links to
301 mantle plume heads. Geological Society of America Special Paper 352, 483-576.
302 Ernst, R.E., Buchan, K.L., Campbell, I.H., 2005. Frontiers in Large Igneous Province
303 research. Lithos 79, 271-297.
304 Ernst, R.E., Liikane, D.A., Jowitt, S.M., Buchan, K.L., Blanchard, J.A., 2019. A new
305 plumbing system framework for mantle plume-related continental Large Igneous
306 Provinces and their mafic-ultramafic intrusions. J. Volcanol. Geotherm. Res. 384,
307 75-84.

Fan, W.M., Wang, Y.J., Zhang, A.M., Zhang, F.F., Zhang, Y.Z., 2010. Permian arc–backarc basin development along the Ailaoshan tectonic zone: geochemical, isotopic and geochronological evidence from the Mojiang volcanic rocks, Southwest China. Lithos 119, 553-568.

Foulger, G.R., 2012. Are ‘hot spots’ hot spots?. Journal of Geodynamics 58, 1-28.

Garfunkel, Z., 1975. Growth, Shrinking, and Long-Term Evolution of Plates and Their Implications for the Flow Pattern in the Mantle. Journal of Geophysical Research 80, 4425-4432.

Griffiths, R.W., Campbell, I.H., 1991. Interaction of mantle plume heads with the Earth’s surface and onset of small-scale convection. J. Geophys. Res. 96, 18295-18310.

He C.S., 2011. Seismic evidence for plume and subducting slab in West Yunnan, Southwestern China. Acta Geologica Sinca 85, 629-636.

He, C.S., Santosh, M., 2017. Mantle roots of the Emeishan plume: An evaluation based on teleseismic P-wave tomography. Solid Earth 8, 1141-1151.

He, C.S., Santosh, M., 2021. Mantle upwelling beneath the Cathaysia Block, South China. Tectonics 40, e2020TC006447.

He, C.S., Santosh, M., Wu, J.P., Chen, X.H., 2014. Plume or no plume: Emeishan Large Igneous Province in Southwest China revisited from receiver function analysis. Physics of the Earth and Planetary Interiors 232, 72-78.

He, C.S., Santosh, M., Dong, S.W., 2015. Continental dynamics of Eastern China: insights from tectonic history and receiver function analysis. Earth-Science Reviews 145, 9-24.

He, C.S., Santosh, M., 2020. Formation of the North–South Seismic Zone and Emeishan Large Igneous Province in Central China: Insights from P-Wave Teleseismic Tomography. Bulletin of the Seismological Society of America.

He, P.L., Huang, X.L., Xu, Y.G., Li, H.Y., Wang, X., Li, W.X., 2016. Plume orogenic lithosphere interaction recorded in the Haladala layered intrusion in the Southwest Tianshan Orogen, NW China. J. Geophys. Res. Solid Earth 121, 1525-1545.

Helffrich, G., 2000. Topography of the transition zone seismic discontinuities. Reviews of Geophysics 38, 141-158.

Hennig, D., Lehmann, B., Frei, D., Belyatsky, B., Zhao, X.F., Cabral, A.R., Zeng, P.S., Zhou, M.F., Schmidt, K., 2009. Early Permian seafloor to continental arc magmatism in the eastern Paleo-Tethys: U-Pb age and Nd\Sr isotope data from the southern Lancangjiang zone, Yunnan, China. Lithos 113, 408-422.

Hou, Z.Q., Zaw, K., Pan, G.T., Mo, X.X., Xu, Q., Hu, Y.Z., Li, X.Z., 2007. Sanjiang Tethyan metallogenesis in S.W. China: tectonic setting, metallogenic epochs and deposit types. Ore Geology Reviews 31, 48-87.

Huang, Z.C., Wang, P., Xu, M.J., Wang, L.S., Ding, Z.F., Wu, Y., Xu, M.J., Mi, N., Yu, D.Y., Li, H., 2015. Mantle structure and dynamics beneath SE Tibet revealed by new seismic images. Earth and Planetary Science Letters 411, 100-111.

Lu, C., Grand, S.P., Lai, H., Garnero, E.J., 2019. TX2019slab: A New P and S Tomography Model Incorporating Subducting Slabs. J. Geophys. Res. 124, 11549-11567.

Ivanov, A.V., Litasov, K.D., 2013. The deep water cycle and flood basalt volcanism. Int.

352 Geol. Rev. 56,1-14.
353 Ivanov, A.V., Demonterova, E.I., Rasskazov, S.V., Yasnygina, T.A., 2008. Low-Ti melts
354 from the Southeastern Siberian Traps Large Igneous Province: Evidence for a
355 water-rich mantle source?. J. Earth Syst. Sci. 117, 1-21.
356 Kennett, B.L.N., Engdahl, E.R., Buland, R., 1995. Constraints on seismic velocities in the
357 Earth from traveltimes. Geophys. J. Int.122, 108-124.
358 Kincaid, C., Druken, K. A., Griffiths, R. W., Stegman, D.R., 2013. Bifurcation of the
359 Yellowstone plume driven by subduction‐induced mantle flow. Nature Geoscience,
360 6(5), 395–399.
361 Kou, C.H., Zhang, Z.C., Santosh, M., Huang, H., Hou, T., Liao, B.L., Li, H.B., 2012. Picritic
362 porphyrites generated in a slab-window setting: Implications for the transition from
363 Paleo-Tethyan to Neo-Tethyan tectonics. Lithos, 155, 375-391.
364 Langston, C.A., 1977. The effect of planar dipping structure on source and receiver
365 responses for constant ray parameter. Bull. Seismol. Soc. Am., 67, 1029-1050.
366 Lei, J.S., Zhao, D., Xu, X.W., Xu, Y.G., Du, M.F., 2019. Is there a big mantle wedge under
367 eastern Tibet?. Physics of the Earth and Planetary Interiors 292, 100-113.
368 Leloup, P.H., Lacassin, R., Tapponnier, P., Schärer, U. Zhong, D.L., Liu, X.H., Zhang, L.S.,
369 Ji, S.C., Trinh, P.T., 1995. The Ailao Shan–Red River shear zone (Yunnan, China),
370 Tertiary transform boundary of Indochina. Tectonophysics 251, 3-84.
371 Liu, C.Y., Zhu, R., 2009. Geodynamic significances of the Emeishan Basalts. Earth
372 Science Frontiers 16, 52-69.
373 Liu, F.T., Liu, J.H., He, J.K., You, Q.Y., 2000. The subducted plate relic of the low Yangtze

374 terrane at the Dianxi Tethyan orogeny. Chinese Science Bulletin 45, 79-84.
375 Liu, W.L., Xia, B., 2015. Age and geochemistry of western Hoh-Xil–Songpan-Ganzi
376 granitoids, northern Tibet: Implications for the Mesozoic closure of the Paleo-Tethys
377 ocean: Comment. Lithos 212-215, 453-456.
378 Metcalfe, I., 2013. Gondwana dispersion and Asian accretion: tectonic and
379 palaeogeographic evolution of eastern Tethys. J. Asian Earth Sci. 66, 1-33.
380 Mo, X.X., Deng, J.F., Dong, F.L., H, Y.X., Wang, Y., Zhou, S., Yang, W.G., 2001. Volcanic
381 petrotectonic assemblages in Sanjiang Orogenic Belt, SW China and implication for
382 tectonics. Geol. J. China Univ. 7, 121-138 (in Chinese with English abstract).
383 Mo, X.X., Shen, S.Y., Zhu, Q.W., 1998. Volcanics–Ophiolite and Mineralization of Middle
384 and Southern Part in Sanjiang, Southern China. Geological Publishing House, Beijing,
385 pp. 1-128 (in Chinese with English abstract).
386 Owens, T.J., Zandt, G., Taylor, S.R., 1984. Seismic evidence for ancient rift beneath the
387 Cumberland plateau, Tenessee: A detailed analysis of broadband teleseismic P
388 waveforms. J. Geophys. Res. 89, 7783-7795.
389 Pan, G.T., Wang, L.Q., Li, R.S., Yuan, S.H., Ji, W.H., Yin, F.G., Zhang, W.P., Wang, B.D.,
390 2012. Tectonic evolution of the Qinghai–Tibet Plateau. J. Asian Earth Sci. 53, 3-14.
391 Peng, T.P., Wilde, S.A., Wang, Y.J., Fan, W.M., Peng, B.X., 2013. Mid-Triassic felsic
392 igneous rocks from the southern Lancangjiang Zone, SW China: Petrogenesis and
393 implications for the evolution of Paleo-Tethys. Lithos 168-169, 15-32.
394 Petersen, K.D., Schiffer, C., Nagel, T., 2018. LIP formation and protracted lower mantle
395 upwelling induced by rifting and delamination. Scientific Reports 16578.

396 Pirajno, F., Hoatson, D.M., 2012. A review of Australia's Large Igneous Provinces and
397 associated mineral systems: Implications for mantle dynamics through geological
398 time. Ore Geology Reviews 48, 2-54.
399 Revenaugh, J., Jordan, T.H., 1991. Mantle layering from SCS reverberations: 3. The
400 upper mantle, J. Geophys. Res. 96 (B12), 19781-19810.
401 Reid, A., Wilson, C.J.L., Shun, L., Pearson, N., Belousova, E., 2007. Mesozoic plutons of
402 the Yidun arc, SW China: U/Pb geochronology and Hf isotopic signature. Ore Geol.
403 Rev. 34, 88-106.
404 Saikia, A., Frost, D.J., Rubie, D.C., 2008. Splitting of the 520-Kilometer Seismic
405 Discontinuity and Chemical Heterogeneity in the Mantle. Science 319, 115-118.
406 Santosh, M., Maruyama, S., Komiya, T., Yamamoto, S., 2010. Orogens in the evolving
407 Earth: from surface continents to ‘lost continents’ at the core-mantle boundary.
408 Geological Society, London, Special Publications 338, 77-116.
409 Sengör, A.M.C., 2001. Elevation as indicator of mantle plume activity. In: Ernst, R.E.,
410 Buchan, K.L. (Eds.), Mantle Plumes: Their Identification Through Time, Special
411 Paper, vol. 352. Geological Society of America, Boulder, CO, pp. 183-225.
412 Shen, L., Yu, J.H., O’Reilly, S.Y., Griffin, W.L., 2018. Tectonic switching of southeast
413 China in the Late Paleozoic. Journal of Geophysical Research: Solid Earth, 123,
414 8508-8526.
415 Song, P.P., Ding, L., Li, Z.Y., Lippert, P.C., Yue, Y.H., 2017. Paleomagnetism of Middle
416 Triassic lavas from northern Qiangtang (Tibet): Constraints on the closure of the
417 Paleo-Tethys Ocean. Earth and Planetary Science Letters 475,119-133.

418 Stefano, C.J., Mukasa, S.B., Andronikov, A., Leeman, W.P., 2011. Water and volatile
419 systematics of olivine-hosted melt inclusions from the Yellowstone hotspot track.
420 Contrib. Mineral. Petrol. 161, 615-633.
421 Strak, V., Schellart, W.P., 2018. A subduction and mantle plume origin for Samoan
422 volcanism. Scientific Reports 8, 10424.
423 Uenzelmann-Neben, G., 2013. Volcanology: Magma giant. Nature Geoscience 6,
424 902-903.
425 Ukstins Peate, I., Bryan, S.E., 2008. Re-evaluating plume-induced uplift in the Emeishan
426 large igneous province. Nature Geoscience 1, 625-629.
427 van der Meijde, M., van der Lee, S., Giardini, D., 2005. Seismic discontinuities in the
428 Mediterranean mantle: Physics of the Earth and Planetary Interiors 148, 233-250.
429 VanDecar, J.C., Crosson, R.S., 1990. Determination of teleseismic relative phase arrival
430 times using multi-channel cross-correlation and least squares. Bull. Seismol. Soc. Am.
431 80, 150-169.
432 Wang, C.M., Deng, J., Carranza, E.J.M., Santosh, M., 2014. Tin metallogenesis
433 associated with granitoids in the southwestern Sanjiang T ethyan Domain: Nature,
434 deposit types, and tectonic setting. Gondwana Research 26, 576-593.
435 Wang, J., Wang, Q., Zhang, C., Dan, W., Qi, Y., Zhang, X.-Z., & Xia, X.-P. (2018). Late
436 Permian bimodal volcanic rocks in the northern Qiangtang Terrane, central Tibet:
437 Evidence for interaction between the Emeishan plume and the Paleo-Tethyan
438 subduction system. Journal of Geophysical Research: Solid Earth, 123, 6540–6561.
439 Weislogel, A.L., 2008. Tectonostatigraphic and geochronologic constraints on evolution of

440 the northeast Paleotethys from the Songpan-Ganzi complex, central China.
441 Tectonophysics 451, 331-345.
442 Wignall, P.B., 2011. Lethal volcanism. Nature 477, 285-286.
443 Wilson, J.T., 1963. A possible origin of the Hawaiian Islands. Canadian Journal of Physics
444 41, 863-870.
445 Wilson, M., 1989. Igneous Petrogenesis. Kluwer Academic Publishers, pp. 325-459.
446 Wu, Y.D., Ren, Z.Y., Handler, M.R., Zhang, L., Qian, S.P., Xu, Y.G., Wang, C.Y., Wang,
447 Y., Chen, L.L., 2018. Melt diversity and magmatic evolution in the Dali Picrites,
448 Emeishan Large Igneous Province. Journal of Geophysical Research: Solid Earth,
449 123, 9635–9657. https://doi.org/10.1029/2018JB015495.
450 Wu, Z., 1994. Thermal structure of crust in eastern Hebei: inferred from petrological model.
451 Geosciences 8, 133-138 (in chinese).
452 Xu, J., Xia, X.P., Lai, C.K., Zhou, M., & Ma, P. (2019). First identification of Late Permian
453 Nb‐enriched basalts in Ailaoshan region (SW Yunnan, China): Contribution from
454 Emeishan plume to subduction of eastern Paleotethys. Geophysical Research
455 Letters, 46, 2511-2523.
456 Xu, M.J., Huang, H., Huang, Z.C., Wang, P., Wang, L.S., Xu, M.J., Mi, N., Li, H., Yu, D.Y.,
457 Yuan, X.H., 2018. Insight into the subducted Indian slab and origin of the Tengchong
458 volcano in SE Tibet from receiver function analysis. Earth and Planetary Science
459 Letters 482, 567-579.
460 Xu, Y., Yang, Z., Tong, Y.B., Jing, X., 2018. Paleomagnetic secular variation constraints
461 on the rapid eruption of the Emeishan continental flood basalts in southwestern China

462 and northern Vietnam. Journal of Geophysical Research: Solid Earth, 123,
463 2597-2617.
464 Xu, Y.G., Chung, S.L., Jahn, B.M., Wu, G.Y., 2001. Petrologic and geochemical
465 constraints on the petrogenesis of Permian–Triassic Emeishan flood basalts in
466 Southwestern China. Lithos 58, 145-168.
467 Xu, Y.G., He, B., Chung, S.L., Menzies, M.A. Frey, F.A., 2004. Geologic, geochemical,
468 and geophysical consequences of plume involvement in the Emeishan flood-basalt
469 province: Geology 32, 917-920.
470 Xu, Z.Q., Dilek, Y., Cao, H., Yang, J.S., Robinson, P., Ma, C.Q., Li, H.Q., Jolivet, M., Roger,
471 F., Chen, X.J., 2015. Paleo-Tethyan evolution of Tibet as recorded in the East
472 Cimmerides and West Cathaysides. Journal of Asian Earth Sciences 105, 320-337.
473 Yang, C., Liu, S.A., 2019. Zinc isotope constraints on recycled oceanic crust in the mantle
474 sources of the Emeishan large igneous province. Journal of Geophysical Research:
475 Solid Earth, 124, 12,537-12,555.
476 Yang, T., Wu, J.P., Wang, W.L., 2014. Complex Structure beneath the Southeastern
477 Tibetan Plateau from Teleseismic P-Wave Tomography. Bulletin of the Seismological
478 Society of America 104, 1056–1069.
479 Zhai, M.G., Fan, Q.C., Zhang, H.F., Sui, J.L., Shao, J.A., 2007. Lower crustal processes
480 leading to Mesozoic lithospheric thinning beneath eastern North China: Underplating,
481 replacement and delamination. Lithos 96, 36-54.
482 Zhang, H.F., Parrish, R., Zhang, L., Xu, W.C., Yuan, H.L., Gao, S., Crowley, Q.G., 2007.
483 A-type granite and adakitic magmatism association in Songpan–Garze fold belt,

eastern Tibetan Plateau: implication for lithospheric delamination. Lithos 97, 323-335.

Zhang, R., Wu, Y., Gao, Z., Fu, Y. V., Sun, L., Wu, Q., Ding, Z., 2017. Upper mantle discontinuity structure beneath eastern and southeastern Tibet: New constraints on the Tengchong intraplate volcano and signatures of detached lithosphere under the western Yangtze Craton, J. Geophys. Res. Solid Earth, 122.

Zhao, D., Hasegawa, A., Horiuchi, S., 1992. Tomographic imaging of P- and S-wave velocity structure beneath northeastern Japan: J. Geophys. Res. 97, 19909-19928.

Zhao, D., Ohtani, E., 2009. Deep slab subduction and dehydration and their geodynamic consequences: evidence from seismology and mineral physics. Gondwana Research 16, 401-413.

Zhu, J., Zhang, Z.C., Santosh, M., Jin, Z.L., 2020. Carlin-style gold province linked to the extinct Emeishan plume, Earth and Planetary Science Letters 530, 115940.

Zhu, L., 2000. Crustal structure across the San Andreas Fault, southern California from teleseismic converted waves. Earth and Planetary Science Letters 179, 183-190.

Zi, J.W., Cawood, P.A., Fan, W.M., Wang, Y.J., Tohver, E., McCuaig, T.C., 2012. Generation of Early Indosinian enriched mantle-derived granitoid pluton in the Sanjiang Orogen (SW China) in response to closure of the Paleo-Tethys. Lithos 140, 166-182.

Additional information

Competing Interests: The authors declare no competing interests.

Electronic supplementary material

Supplementary Information

Figure captions:

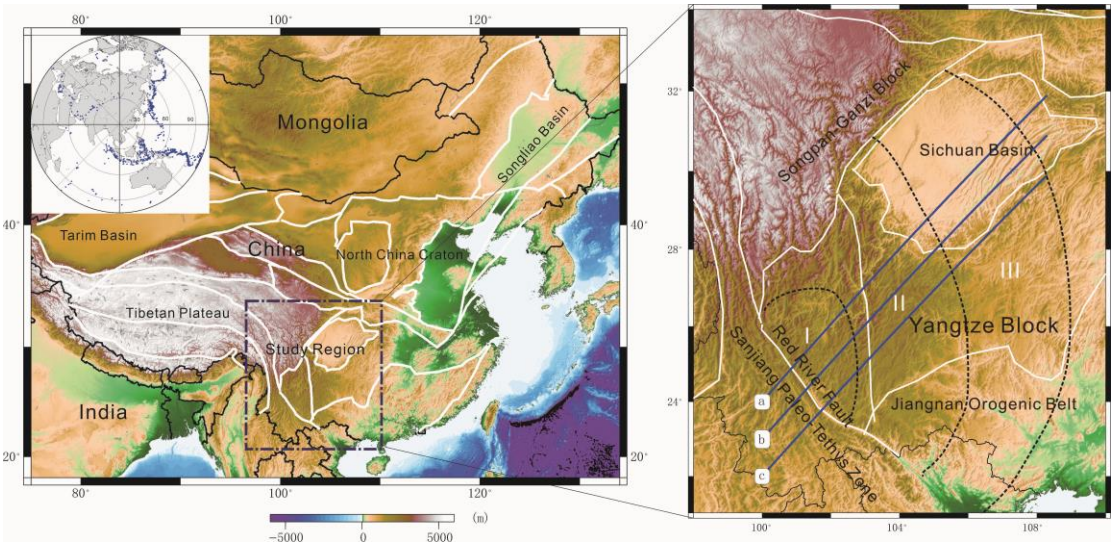

Fig. 1. The location of the study region. White lines: tectonic boundaries; black triangles: seismic stations; black dotted lines: boundaries of the inner, middle and outer zones of the ELIP (I: inner zone; II: middle zone; III: outer zone); blue lines: overlapping profiles of P-wave velocity perturbations and CCP stacking of receiver functions. Upper corner of left panel (insert figure): distribution of teleseismic events collected from the China Earthquake Network in this study, which yields reasonable coverage at the different azimuthal angles.

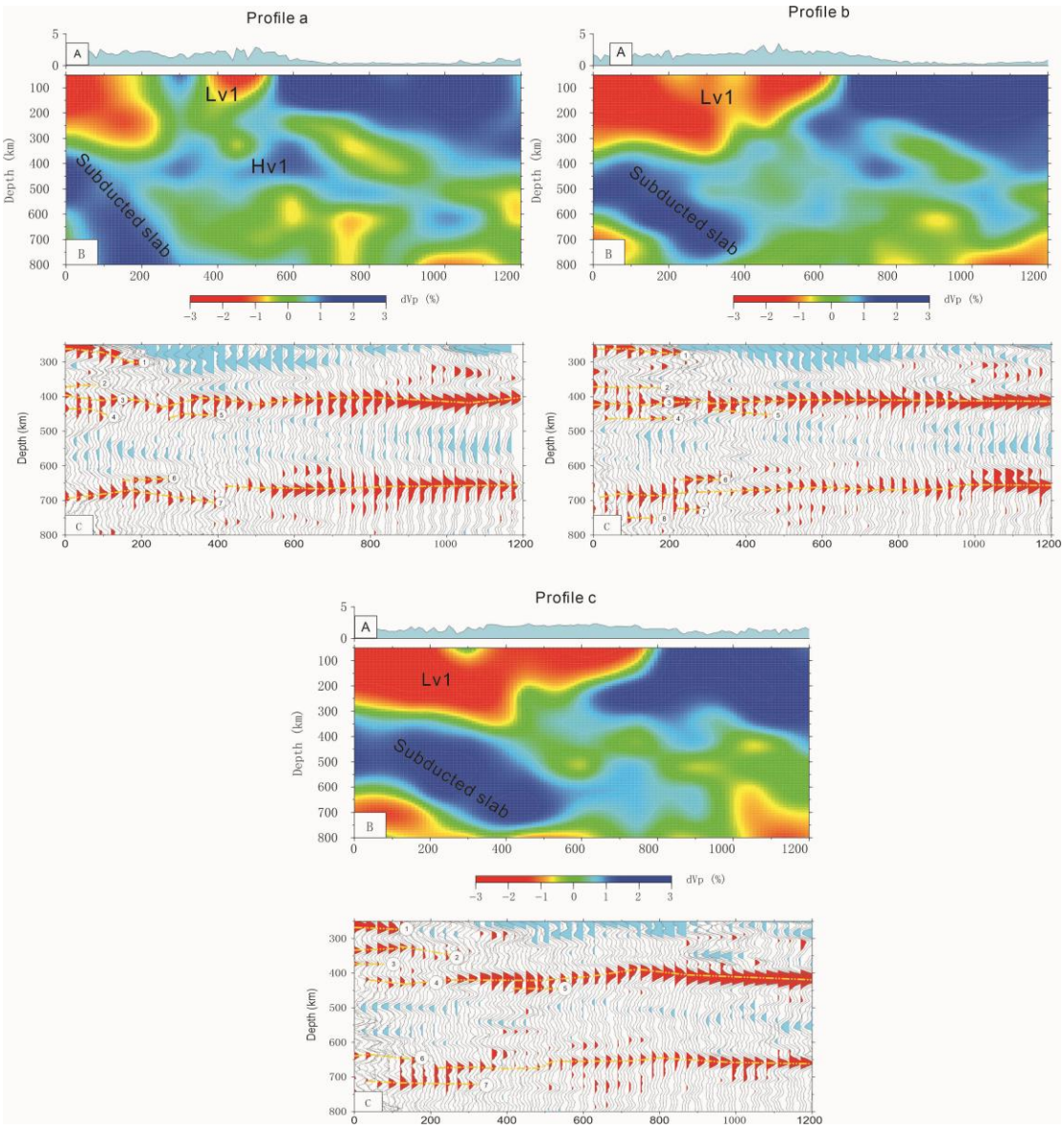

Fig. 2. Profile a, b and c (location of the profiles, see Fig. 1). A: topographic profile; B: P-wave velocity perturbation profile (He and Santosh, 2020); C: CCP stacking of receiver function profile. The bootstrapping method is used to calculate the stacked amplitudes (resampling 2000 times in the dataset), and the 95% confidence level is used to calculate the final mean receiver functions (middle lines). ①: X-discontinuity; ②, ③, ④ and ⑤: split 410 km discontinuity;⑥, ⑦ and ⑧: split 660 km discontinuity or deepening 660 km discontinuity.

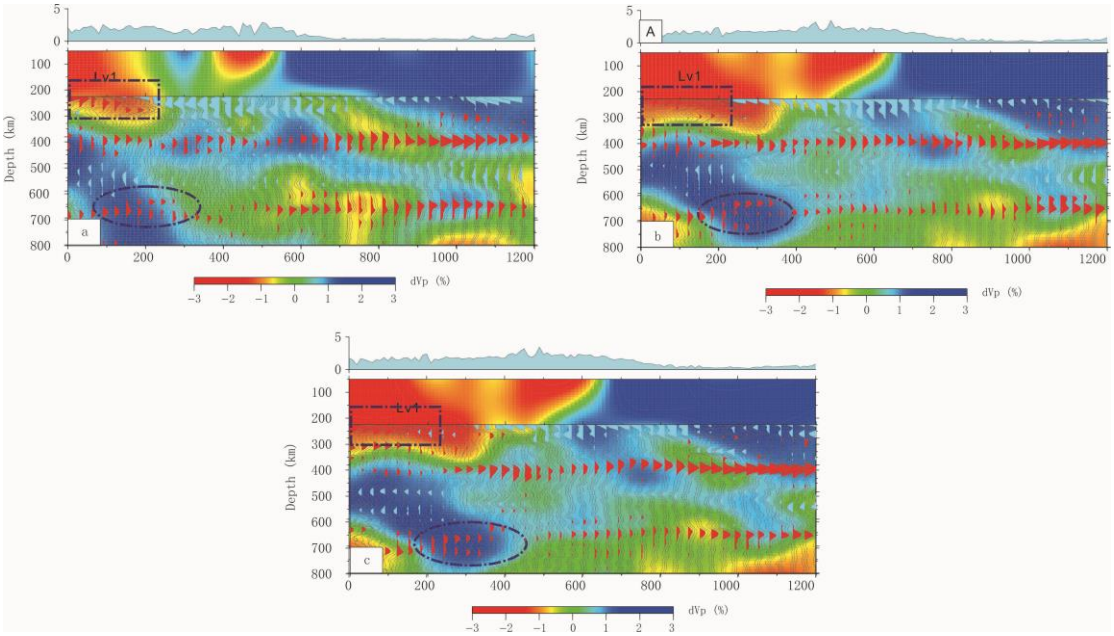

526

527 Fig. 3. Profile a, b and c. Composite picture of the CCP stacking of receiver functions and

528 P-wave velocity perturbation. The deepening of the 660 km discontinuity or split 660 km

529 discontinuity corresponding to the location of the subducted slab (the region within the

530 blue ellipse). X-discontinuity corresponding to the location of the low-velocity anomaly

531 (Lv1) (the region within the blue rectangle). Horizontal coordinate: km.

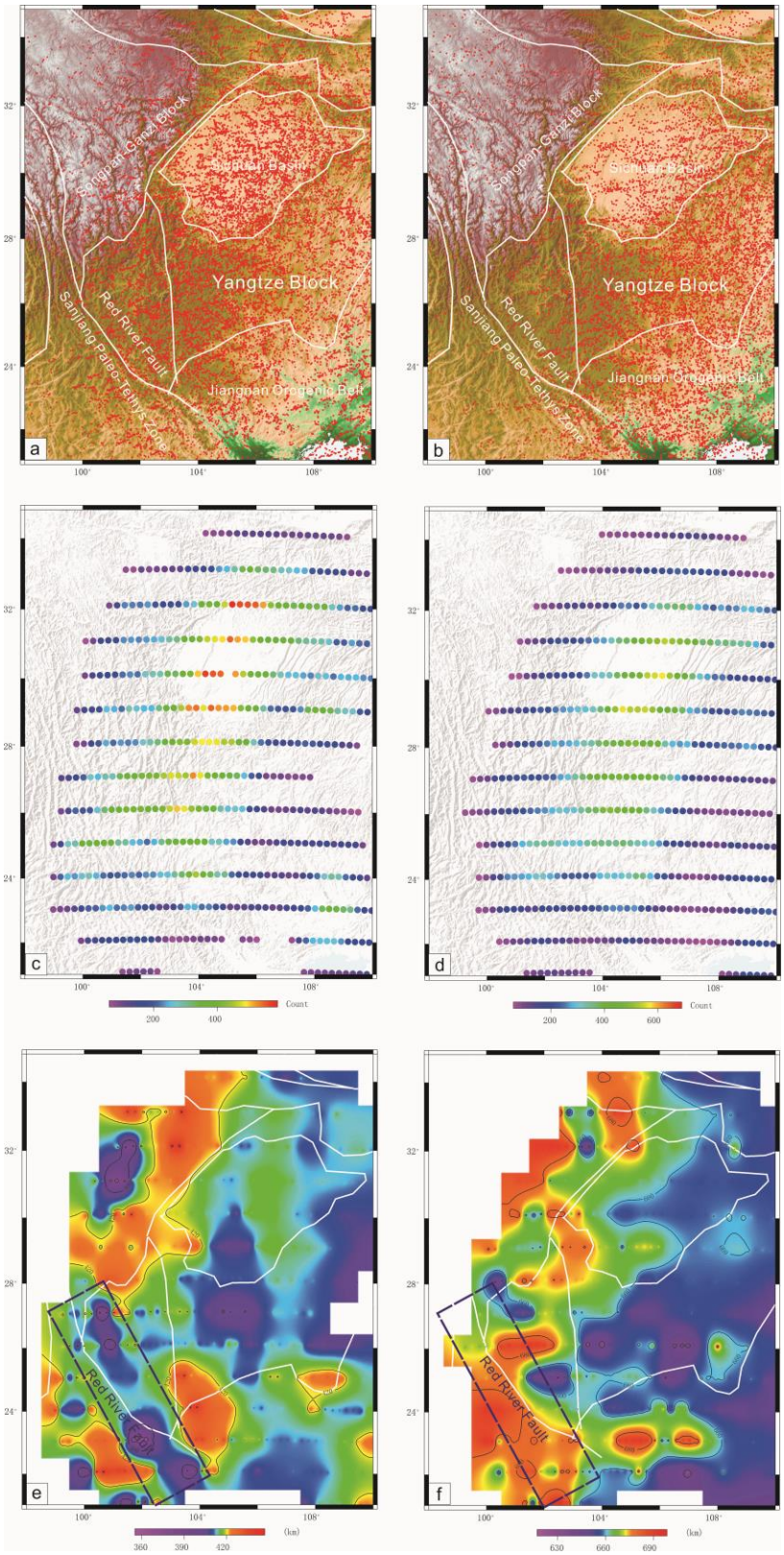

Fig. 4. Topographies of the 410 and 660 km discontinuities. Piercing points at 410 km depth (a) and 660 km depth (b), red point: piercing points. CCP stacking points of mean receiver function at 410 km discontinuity (c) and 660 km discontinuity (d), sample point:

536 the latitudinal interval is 25 km and longitudinal interval is 1° , the bootstrapping method is
537 used to calculate the stacked amplitudes (resampling 2000 times in the dataset), and the
538 95% confidence level is used to calculate the final mean receiver functions and the
539 number of stacking amplitude points is greater than 60 (c and d). Depths of the 410 km
540 discontinuity (e) and 660 km discontinuity (f), which have been corrected on the basis of a
541 global 3-D local velocity model (Lu et al., 2019).

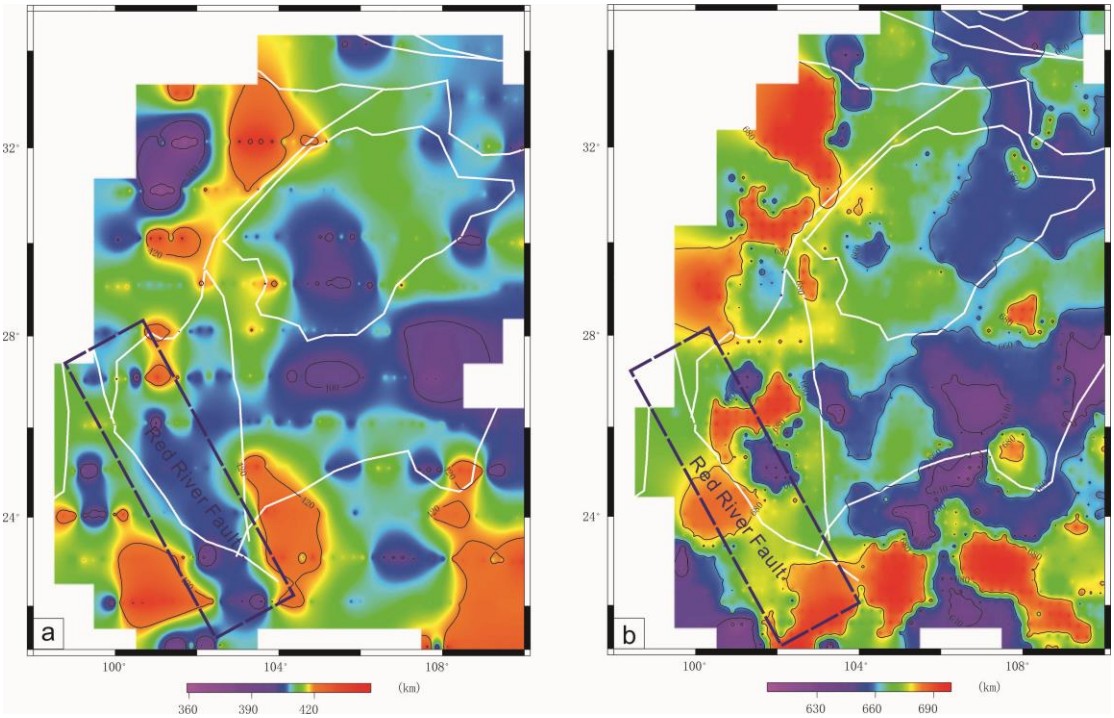

542

543 Fig. 5. Topography of 410 km discontinuity (a) and 660 km discontinuity, which have been
544 corrected on the basis of a local 3-D local velocity model (He and Santosh, 2020). The
545 bootstrapping method is used to calculate the stacked amplitudes (resampling 2000 times
546 in the dataset), and the 95% confidence level is used to calculate the final mean receiver
547 functions and the number of stacking amplitude points is greater than 60. Sample point:
548 the latitudinal interval is 25 km and longitudinal interval is 1° .

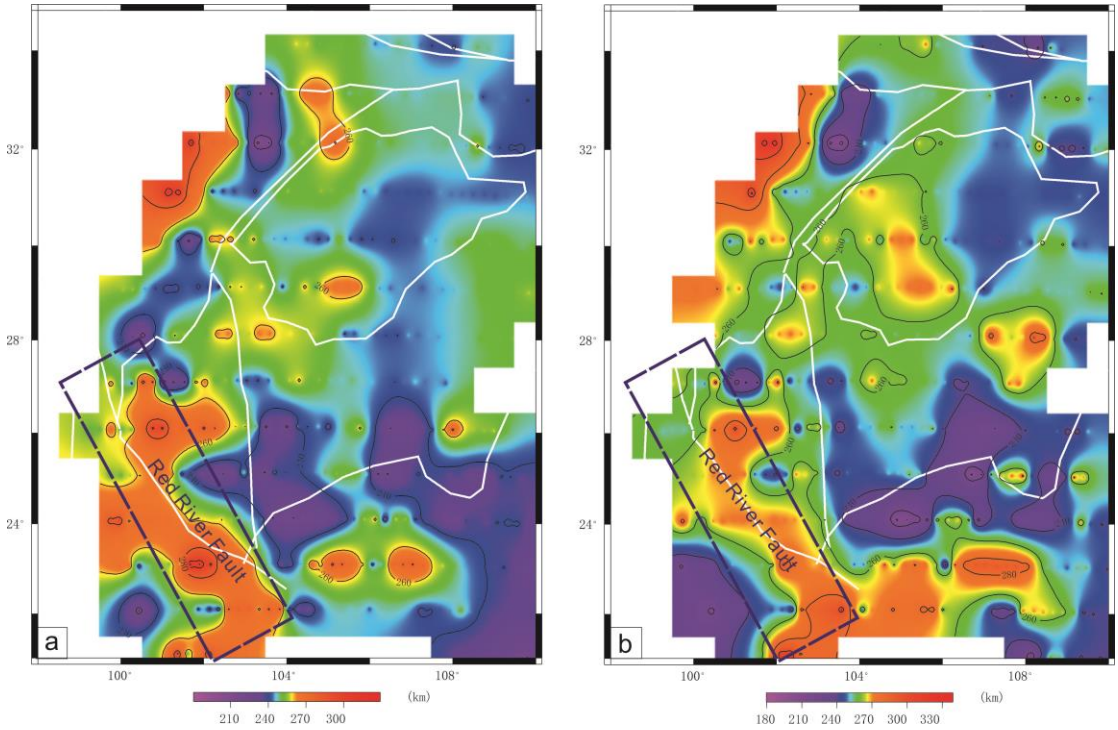

549

550 Fig. 6. Thickness of the MTZ extracted from a global 3-D velocity model (Lu et al., 2019)

551 (a) and the thickness of the MTZ extracted from a local 3-D velocity model (He and

552 Santosh, 2020) (b). The bootstrapping method is used to calculate the stacked amplitudes

553 (resampling 2000 times in the dataset), and the 95% confidence level is used to calculate

554 the final mean receiver functions and the number of stacking amplitude points is greater

555 than 60. Sample point: the latitudinal interval is 25 km and longitudinal interval is 1° .

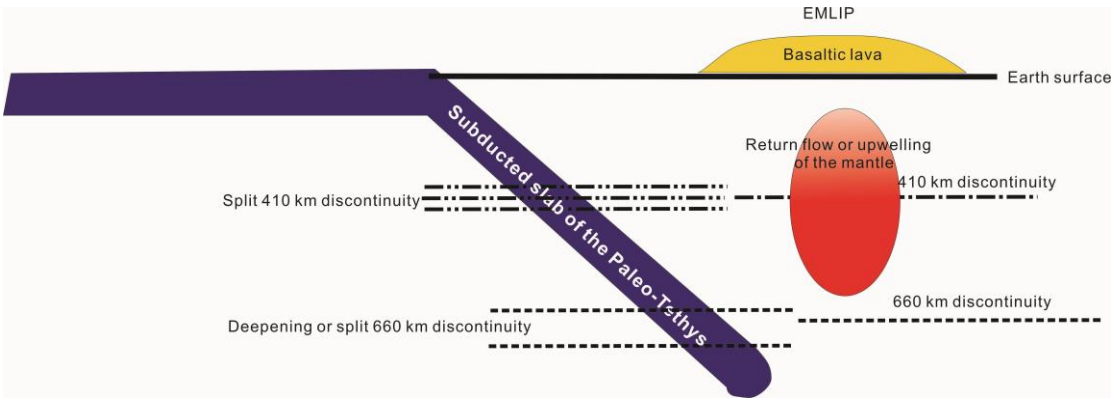

556

557 Fig. 7. Sketch of the model for the subducted OLPT, which might induce large-scale return

558 flow or upwelling of the mantle and lead to the formation of the ELIP.